Autonomous Optical Navigation for Earth-Observing Satellites Using Coastline Matching

Miranda N. Straub* and John A. Christian†

West Virginia University, Morgantown, WV, 26506

In order to meet the demands of future space missions, it is beneficial for spacecraft to have the capability to support autonomous navigation. This is true for both crewed and uncrewed vehicles. For crewed vehicles, autonomous navigation would allow the crew to safely navigate home in the event of a communication system failure. For uncrewed missions, autonomous navigation reduces the demand on ground-based infrastructure and could allow for more flexible operation. One promising technique for achieving these goals is through optical navigation. To this end, the present work considers how camera images of the Earth's surface could enable autonomous navigation of a satellite in low Earth orbit. Specifically, this study will investigate the use of coastlines and other natural land-water boundaries for navigation. Observed coastlines can be matched to a pre-existing coastline database in order to determine the location of the spacecraft. This paper examines how such measurements may be processed in an on-board extended Kalman filter (EKF) to provide completely autonomous estimates of the spacecraft state throughout the duration of the mission.

Nomenclature

$\mathbf{x}$ State Vector
$\mathbf{y}$ Measurement Vector
$\mathbf{P}$ State Covariance Matrix
$\mathbf{F}$ Jacobian Matrix
$\mathbf{Q}$ Process Noise Covariance Matrix
$\mathbf{H}$ Measurement Sensitivity Matrix
$\mathbf{K}$ Kalman Gain
$\mathbf{R}$ Measurement Covariance Matrix
$\mathbf{r}$ Spacecraft Position Vector
$\mathbf{s}$ Vector from spacecraft to observed landmark
$\mathbf{o}$ Vector from center of Earth to observed landmark
$\mathbf{e}$ Unit vector in direction of observed landmark
$\mathbf{T}$ Rotation Matrix
μ Gravitational Parameter

I.   Introduction

With the many recent technological developments in the aerospace industry and the desire to conduct more ambitious space missions, there is an increasing need for fully autonomous spacecraft. Autonomous spacecraft navigation systems are important for both crewed and uncrewed missions. In the case of crewed

---

*Graduate Research Assistant, Department of Mechanical and Aerospace Engineering, Benjamin M. Statler College of Engineering and Mineral Resources.

†Assistant Professor, Department of Mechanical and Aerospace Engineering, Benjamin M. Statler College of Engineering and Mineral Resources, and AIAA Senior Member.

American Institute of Aeronautics and Astronautics

missions, autonomous navigation systems are crucial in bringing the crew home safely in case of a communication system failure. For robotic missions, autonomous navigation reduces demands on ground-based infrastructure and increases mission flexibility when far away from the Earth. For either scenario, previous work has shown optical navigation (OPNAV) to be one method of fulfilling the need for autonomous navigation.[1]

The process of OPNAV includes capturing an image of a known object and using the information in this image to determine the location of the spacecraft. Target bodies for optical navigation include planets, moons, asteroids, comets, and stars.[2] At long ranges, it is common to use horizon-based OPNAV techniques. At closer ranges, surface features may be observed. On Earth, there are a number of different naturally occurring features that could be used for navigation. Of special interest here are coastlines, islands, and other inland water boundaries such as lakes and rivers.[3] Thus, the focus of this paper will be on autonomous optical navigation of a satellite in low-Earth orbit (LEO) using coastlines as landmarks.

For this study, it is assumed that the only source of external measurements will be from a star-tracker (for attitude) and from an Earth-observing camera. The state of the spacecraft will be propagated on-board using assumed dynamics and Inertial Measurement Unit (IMU) data. In addition, a camera measurement model will be developed to utilize measurements obtained from landmark observations to be processed in an on-board extended Kalman filter (EKF). These models will be discussed in detail later in the paper.

I.A. Navigation Using Landmarks

Many studies have been carried out concerning the use of optical navigation with various types of surface landmarks.[4–8] For example, craters commonly found on the surface of planets, satellites, asteroids, and other solar system bodies are often proposed as landmarks for optical navigation. Generally, a crater can be identified in an image by looking for an elliptical rim and a bright to dark shading pattern depending on the lighting at the time of observation. Because of these commonalities, most crater detection algorithms consist of a series of steps that include edge detection and ellipse fitting. Once the ellipses are identified as landmarks, the size, shape, and position of that landmark relative to other landmarks are used to match the ellipses with a known database of craters for that body.[6] It should be noted, however, that this process can be difficult because the craters often have different appearances when viewed from different directions and with different sun angles. Also, the age of the crater may contribute to the sharpness of the crater edges on the surface which can make detection easier or more difficult.[4] Techniques such as image cross-correlation, context based matching, and projective conic invariants can be used to make up for these differences but are beyond the scope of this paper. They are discussed in detail in [4] and [8].

Due to the previously mentioned irregularities seen in crater detection, and because craters are less numerous on the Earth's surface, bodies of water can also be used as landmarks for spacecraft orbiting Earth in LEO. This is easily observed due to the contrast in colors between land and water as seen by the spacecraft. These bodies of water can include coastlines, islands, rivers, and lakes. Additional features can be detected as well (e.g. volcanoes, mountains, snow, and even urban areas); however these are often changing over time and can be more difficult to distinguish and map.[9]

I.B. Coastline Determination

Numerous methods of extracting coastlines from images have been studied. Common solutions include using conventional image processing boundary detection methods or classifying illumination levels of an image. When using boundary or edge detection, various methods are available and produce similar results depending on the situation. One popular choice for edge detection is the Canny edge detector.[10] Previous work by Liu and Jezek,[3] however, has shown Canny edge detection to be insufficient for coastline extraction due to the lack of consistent intensity contrast between land and water regions, often resulting in discontinuous coastline data. To alleviate this problem, image segmentation and post-segmentation processing were used in [3]. Other authors, such as those in [11], use two masking steps in addition to the Canny edge detection: an edge focusing step and a closing step used as an input for the object-oriented matching process. The usage of these masking steps in [11] show significant improvements over Canny edge detection.

One other problem that arises with coastline extraction and feature selection is the potential for misidentification of non-coastline boundaries as coastlines. For example, many edge detection techniques use contrast as a determining factor to differentiate boundaries and edges. If the satellite image contains cloud coverage,

American Institute of Aeronautics and Astronautics

it is possible for clouds to be considered boundaries and therefore identified as a possible coastline. A solution to this problem is discussed in [12] using a global ocean color sensor which measures radiances in eight visible and near-infrared bands. By creating scatter plots of radiance observed from two different bands, it was possible to normalize the data and specify thresholds to classify observed regions as land, water, clouds, or ice.

I.C.   Georeferenced Database

A few options are available to provide a reference of coastlines for optical navigation. One of the most well-known databases is provided by the National Geophysical Data Center (NGDC), part of the National Oceanic and Atmospheric Administration (NOAA). World shorelines are provided through the Global Self-Consistent, Hierarchical, High-resolution Geography Database (GSHHG) in the form of shapefiles that store geometrical characteristics of datasets as vector coordinates, i.e. coastlines and other water/land boundaries.[13] These files are able to be read and written using a variety of programs. The NGDC provides a software called GEODAS-NG that has the capability of reading the coastline data from the GSHHG or writing shapefiles from a provided input image.

It is also possible to use MATLAB as a georeferenced database in conjunction with the GSHHG database. MATLAB is capable of plotting low resolution GSHHG data with respect to latitude and longitude coordinates. Using this data, MATLAB was used to construct a model of the Earth to simulate the view of Earth of a satellite in LEO. The footprint simulation was modeled under the assumption that the on-board camera is always nadir-pointing. With this assumption, the spacecraft orbit was propagated using two-body orbital mechanics.[14] Fig. 1 provides a visual representation of a spacecraft in a 1,000 km orbit with a 56°inclination. The solid line represents the ground track of the spacecraft while the gray boxes show the area visible in the camera FOV assuming an image is taken once every 5 minutes.
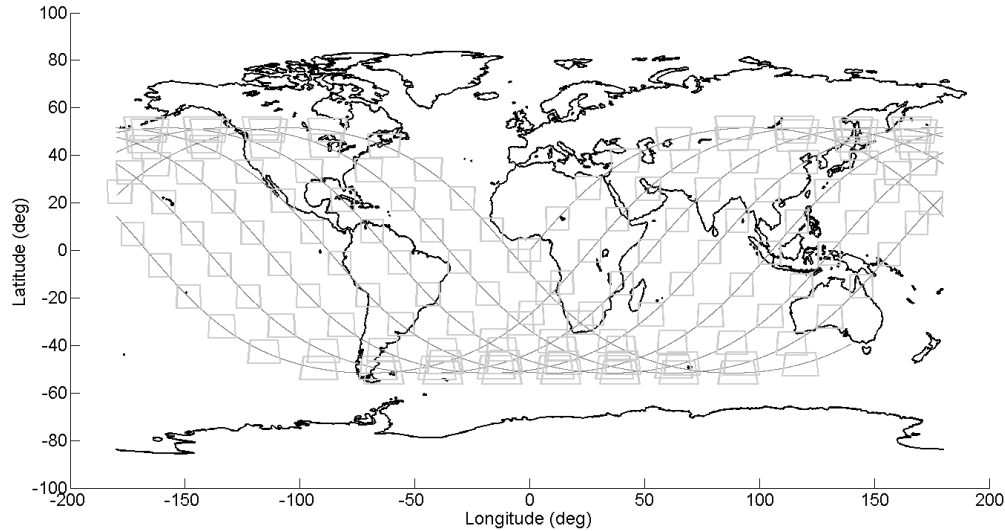

Figure 1: Camera footprints (gray boxes) from a spacecraft in a 56°inclination, 1,000 km circular orbit with images taken once every 5 minutes. The camera has a FOV of 30°.

The ground projected field-of-view (GFOV) can be calculated based on the geometry of the spacecraft position and desired field-of-view (FOV) of the camera,

$$\text{GFOV} = 2h \tan\left(\frac{\text{FOV}}{2}\right) \tag{1}$$

where h is the spacecraft altitude. A 30° FOV was chosen resulting in a viewable footprint of approximately 536 km. A visual representation of the relative size of this footprint as seen by a camera can be seen in Fig. 2a which shows a portion of the Great Lakes.

American Institute of Aeronautics and Astronautics

(a) Simulated satellite image incorporating a camera with a 30°FOV in a 1,000 km circular polar orbit. The blue lines represent the coastline data.
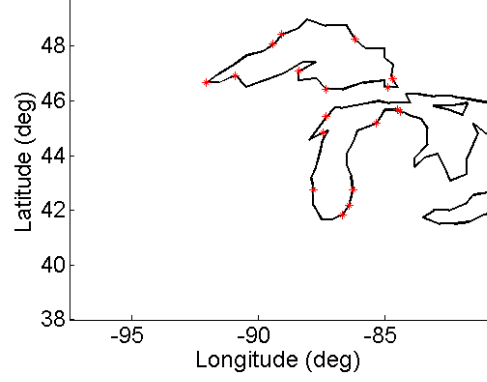
(b) View of coastlines showing exact footprint with various identified coastline points (*) within the spacecraft FOV.

Figure 2: Simulated view of coastlines and the corresponding footprint based on a 1,000 km circular polar orbit.

II.   Mathematical Models

In order to create an algorithm for optical navigation, it is necessary to understand the mathematical models describing the state of the spacecraft as well as the camera model. These models are described in the following sections.

II.A.   Extended Kalman Filter

Due to the nonlinear nature of spacecraft dynamics and optical measurements, an extended Kalman filter (EKF) will be used to estimate the state of the system.[15, 16] The key equations are now briefly reviewed.

Suppose we have a nonlinear system model for state $\dot{\mathbf{x}}$ governed by

$$\dot{\mathbf{x}} = \mathbf{f}(\mathbf{x}, t) + \mathbf{v} \tag{2}$$

where $\mathbf{v}$ is zero mean white noise. The covariance matrix, $\mathbf{P}$, of such a system may be propagated by

$$\dot{\mathbf{P}} = \mathbf{F}\mathbf{P} + \mathbf{P}\mathbf{F}^T + \mathbf{Q} \tag{3}$$

where

$$\mathbf{F}(t) = \left. \frac{\partial \mathbf{f}(\mathbf{x}, t)}{\partial \mathbf{x}} \right|_{\mathbf{x}=\hat{\mathbf{x}}} \tag{4}$$

and $\mathbf{Q}$ is the process noise. Further suppose that at some time, t_k, a new measurement becomes available that is described by

$$\tilde{\mathbf{y}}_k = \mathbf{h}(\mathbf{x}_k) + \mathbf{u}_k \tag{5}$$

where $\mathbf{u}_k \sim \mathcal{N}(0, \mathbf{R}_k)$ and $\mathbf{h}(\mathbf{x})$ is the nonlinear measurement model, described in detail in Section II.C.

Both the *a posteriori* state and covariance estimates, $\hat{\mathbf{x}}_k^+$ and $\mathbf{P}_k^+$, may now be computed by

$$\hat{\mathbf{x}}_k^+ = \hat{\mathbf{x}}_k^- + \mathbf{K}_k(\tilde{\mathbf{y}}_k - \mathbf{h}(\hat{\mathbf{x}}_k^-)) \tag{6}$$

$$\mathbf{P}_k^+ = (\mathbf{I} - \mathbf{K}_k\mathbf{H}_k)\mathbf{P}_k^-(\mathbf{I} - \mathbf{K}_k\mathbf{H}_k)^T + \mathbf{K}_k\mathbf{R}_k\mathbf{K}_k^T \tag{7}$$

where $\mathbf{H}_k$ is the measurement sensitivity matrix,

$$\mathbf{H}_k \triangleq \left. \frac{\partial \mathbf{h}(\mathbf{x})}{\partial \mathbf{x}} \right|_{\mathbf{x}=\hat{\mathbf{x}}} \tag{8}$$

Finally, the optimal update is achieved when $\mathbf{K}_k$ is chosen to be the Kalman gain, where

$$\mathbf{K}_k = \mathbf{P}^-\mathbf{H}_k^T(\mathbf{H}_k\mathbf{P}\mathbf{H}_k^T + \mathbf{R}_k)^{-1} \tag{9}$$

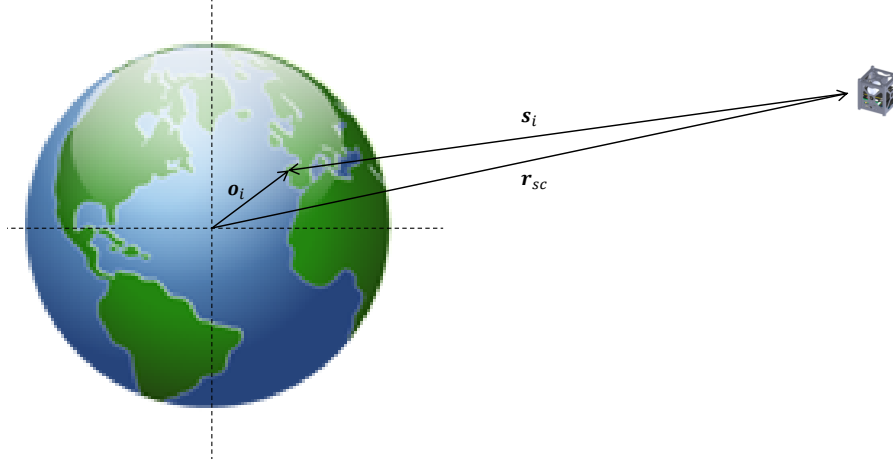American Institute of Aeronautics and Astronautics

Figure 3: Line-of-sight vectors for measurement model.

II.B.   State Propagation using an Extended Kalman Filter

To estimate the state of the spacecraft, the dynamics can be expressed using two-body problem orbital mechanics. The resulting equations of motion for the spacecraft are described by

$$\ddot{\mathbf{r}} = \frac{-\mu}{\|\mathbf{r}\|^3}\mathbf{r} \tag{10}$$

Rewriting in state-space form leads to the following expression for $\mathbf{f}(\mathbf{x}, t)$

$$\mathbf{x} = \begin{bmatrix} \mathbf{r} \\ \dot{\mathbf{r}} \end{bmatrix} \tag{11}$$

$$\mathbf{f}(\mathbf{x}, t) = \begin{bmatrix} \dot{\mathbf{r}} \\ \frac{-\mu}{\|\mathbf{r}\|^3}\mathbf{r} \end{bmatrix} \tag{12}$$

Because $\ddot{\mathbf{r}}$ is nonlinear in $\mathbf{r}$, $\dot{\mathbf{x}}$ must be linearized to first order about the estimate to find $\mathbf{F}(t)$,

$$\mathbf{F}(t) = \frac{\partial \mathbf{f}(\mathbf{x}, t)}{\partial \mathbf{x}}\bigg|_{\mathbf{x}=\hat{\mathbf{x}}} = \begin{bmatrix} \frac{\partial \dot{\mathbf{r}}}{\partial \mathbf{r}} & \frac{\partial \dot{\mathbf{r}}}{\partial \dot{\mathbf{r}}} \\ \frac{\partial \ddot{\mathbf{r}}}{\partial \mathbf{r}} & \frac{\partial \ddot{\mathbf{r}}}{\partial \dot{\mathbf{r}}} \end{bmatrix} = \begin{bmatrix} 0_{3\times3} & \mathbf{I}_{3\times3} \\ \frac{-\mu}{\|\hat{\mathbf{r}}\|^3}\mathbf{I}_{3\times3} + \frac{-\mu}{\|\hat{\mathbf{r}}\|^5}\hat{\mathbf{r}}\hat{\mathbf{r}}^T & 0_{3\times3} \end{bmatrix} \tag{13}$$

Since both $\dot{\mathbf{x}}$ and $\dot{\mathbf{P}}$ are now known, each can be integrated to propagate to a new *a priori* estimate of the state and covariance, $\hat{\mathbf{x}}_k^-$ and $\hat{\mathbf{P}}_k^-$, which are then updated by the EKF.

II.C.   Measurement Model for Coastline Points in Images

Line-of-sight (LOS) measurements are produced from the images obtained by the spacecraft's camera. These measurements are a nonlinear function of the spacecraft state and may be determined by the geometry between the Earth and the spacecraft. From Fig. 3, it is clear that the following geometric relations are obtained by

$$\mathbf{s}_i = \mathbf{o}_i - \mathbf{r}_{sc} \tag{14}$$

$$\mathbf{e}_{iI} = \frac{\mathbf{s}_i}{\|\mathbf{s}_i\|} \tag{15}$$

where $\mathbf{r}_{sc}$ is the position of the spacecraft from the center of the earth, $\mathbf{s}_i$ is the vector from the spacecraft to the ith observed point, or landmark, and $\mathbf{o}_i$ is the vector from the center of the earth to the landmark. The measurement model for a single observed coastline point can then be described as

$$\mathbf{h}(\mathbf{x}) = \mathbf{e}_{iC} = \mathbf{T}_C^I \mathbf{e}_{iI} = \mathbf{T}_C^I \frac{\mathbf{s}_i}{[\mathbf{s}_i^T \mathbf{s}_i]^{1/2}} \tag{16}$$

American Institute of Aeronautics and Astronautics

where $\mathbf{T}_C^I$ is the rotation matrix from the inertial frame to the camera frame. A good estimate of $\mathbf{T}_C^I$ is assumed to be available from a star tracker. From here, the measurement sensitivity matrix may be computed as

$$\mathbf{H}_i = \mathbf{T}_C^I \frac{1}{\|\mathbf{s}_i\|} \left[\{\mathbf{e}_{iI}\mathbf{e}_{iI}^T - \mathbf{I}_{3\times3}\} \quad \mathbf{0}_{3\times3} \right] \tag{17}$$

Additionally, the covariance for a unit vector (LOS) measurement is given by [17] as

$$\mathbf{R}_i = E[(\mathbf{e}_{iC} - \bar{\mathbf{e}}_{iC})(\mathbf{e}_{iC} - \bar{\mathbf{e}}_{iC})^T] \approx \sigma_\Theta^2(\mathbf{I}_{3\times3} - \bar{\mathbf{e}}_{iC}\bar{\mathbf{e}}_{iC}^T) \tag{18}$$

It should be noted that in order to calculate the Kalman gain, as seen in Eq. 9, the quantity $\mathbf{H}_i\mathbf{PH}_i^T + \mathbf{R}_i$ must be invertible. In this particular case, the null space of the measurement covariance, $\mathbf{R}_i$, is the same as the null space of $\mathbf{H}_i\mathbf{PH}_i^T$ assuming $\mathbf{R}_i$ is as seen in Eq. 18. Therefore, a modified version of $\mathbf{K}_i$ is used,

$$\mathbf{K}_i = \mathbf{P}^-\mathbf{H}_i^T(\mathbf{H}_i\mathbf{PH}_i^T + \mathbf{R}_i + \nu\mathbf{e}_i\mathbf{e}_i^T)^{-1} \tag{19}$$

As explained in [18], this does not change the value of $\mathbf{K}_i$ since it is equivalent to adding a $\mathbf{0}$ to the overall equation,

$$\mathbf{H}_i^T\mathbf{e}_i = 0 \tag{20}$$

III.   Simulation Results

III.A.   Coastline Visibility

For this simulation, it is important to ensure that coastlines will be visible based on the spacecraft's orbit and camera parameters. Therefore, simulations were run to determine the percentage of time coastlines would be visible from the spacecraft's position in a 1,000 km orbit with varying inclinations. For simplicity, other orbital parameters, including the right ascension of the ascending node, the argument of periapsis, and the true anomaly, were fixed at 0°. Fig. 4 shows the results of the simulations given various orbital inclinations and camera FOV. It is important to note that these results are orbit-specific and will vary slightly due to differences in orbital parameters, especially attitude. Consequently, the rate at which images are captured also plays a key role in determining how often coastlines are observable. For these results, images are captured once every 30 seconds for a total of 24 hours.
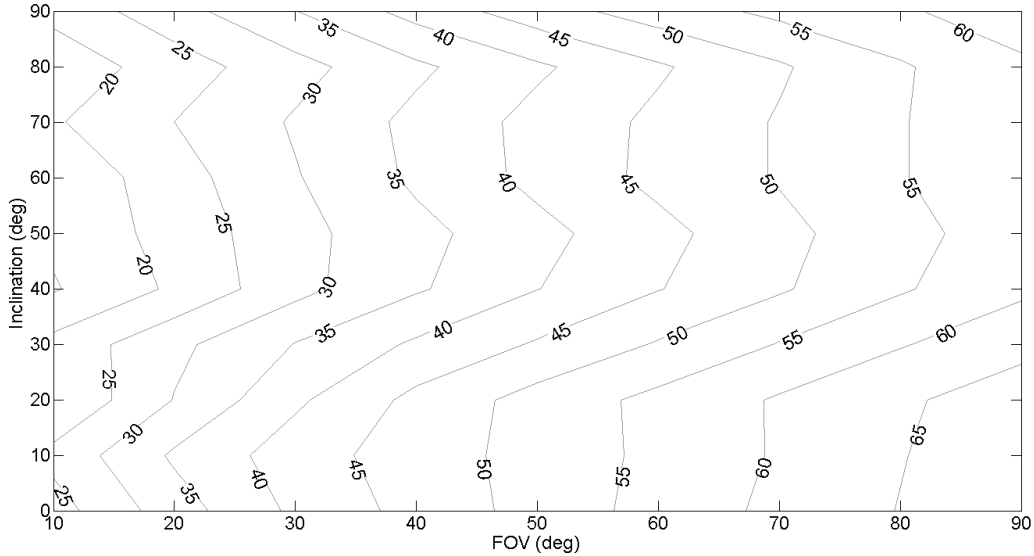

Figure 4: Orbit-specific contour plot showing the percentage of time coastline is observable based on inclination and FOV at a 1,000 km circular orbit with images taken once every five minutes.

III.B. Assessment of Navigation Filter Performance

A Monte Carlo analysis was run to asses the performance of the EKF using only coastline observations. In this case, the initial state was dispersed for each run in the Monte Carlo in a manner consistent with the initial state covariance (standard deviation of 500 m in position and 5 mm/s in velocity). This allowed us to verify that the covariance predicted by the filter is statistically consistent within the Monte Carlo numerical results.

This simulation was carried out for a total of 1,000 runs for each of five orbits (0°, 45°, and 90°, each at 1,000 km altitude, and 45°and 90°at 500 km altitude) to determine the steady state error achievable for each scenario. The additional orbital parameters of these orbits, such as the right ascension of the ascending node, the argument of periapsis, and the true anomaly, were fixed at 0°for simplicity. It is important to note that altering these values will change how often coastlines are able to be detected and results will deviate from those shown in Fig. 4. The following figures show that in all scenarios, the covariance predicted by the filter (gray lines) is consistent with the true covariance (black lines) and that the errors lie well within the 3σ bounds of the covariance.

Comparing Fig. 5 through Fig. 7b, it is apparent where measurements were not present, i.e. where the camera was not able to detect coastlines. However, in all simulated orbits, coastlines appear to have been available at all measurements, hence the constant convergence of the covariance towards steady state. Table 1 provides a summary of the results from the three orbits mentioned above, as well as an additional orbit at 45°inclination and 500 km altitude. Results show that spacecrafts in polar orbits produce the smallest steady state errors. This is likely due to the nearly full-global coverage and corresponding unique coastline points available for camera measurements.

Table 1: Summary of position and velocity errors for specified orbits.

Inclination	Altitude [km]	Along-track Steady State Position Error [km]	Cross-track Steady State Position Error [km]	Radial Steady State Position Error [km]	Along-track Steady State Velocity Error [m/s]	Cross-track Steady State Velocity Error [m/s]	Radial Steady State Velocity Error [m/s]
0°	1,000	1.0	1.4	5.0	5.0	1.4	1.0
45°	1,000	1.0	1.4	5.0	5.0	1.4	1.0
90°	1,000	0.6	1.3	3.0	3.0	1.3	0.6
45°	500	1.0	1.4	4.5	4.8	1.5	1.1
90°	500	0.5	1.3	1.8	2.0	1.4	0.6

IV.   Conclusion

An extended Kalman filter was used to autonomously determine the accuracy in which a spacecraft's position and velocity could be estimated through camera observations of coastlines on Earth's surface. If a coastline is visible, an image processing algorithm is able to match it with a database of known coastline locations. These coordinates are input into the filter to determine the spacecraft's position and velocity steady state error. The results in Table 1 show that based on these simulations, spacecraft in polar orbits are likely to have smaller steady state errors in both position and velocity measurements. Future work related to this topic includes creating an appropriate image processing algorithm able to extract the required information from sample satellite images. It is hoped that this can be implemented on-board a CubeSat launched as part of West Virginia University's proposed WATSON (WVU Advanced Technology Satellite for Optical Navigation) mission in the near future.
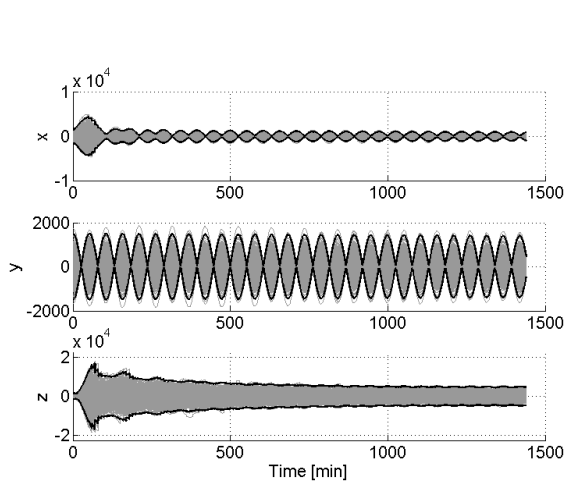
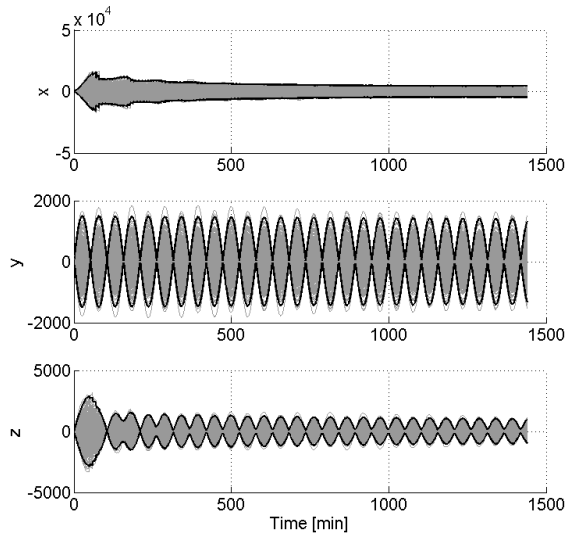American Institute of Aeronautics and Astronautics
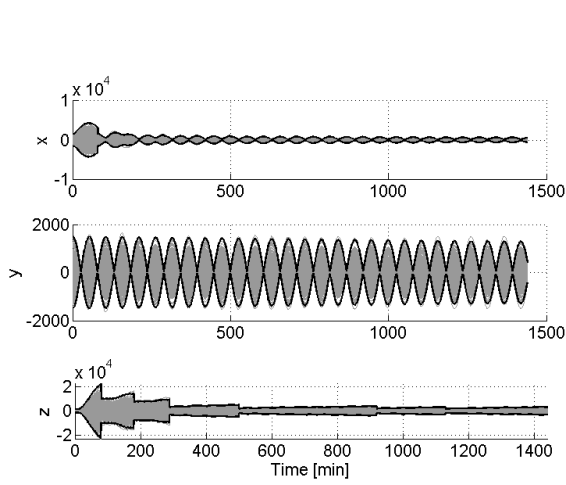
(a) Position error [m] at i=0°.
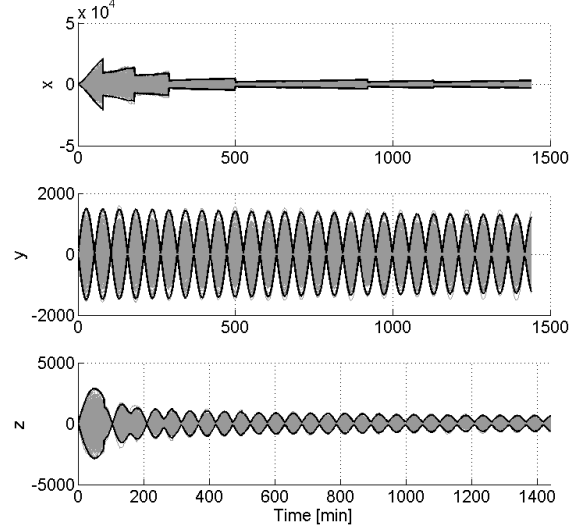
(b) Velocity error [mm/s] at i=0°.

Figure 5: Monte Carlo position and velocity errors at 1,000 km equatorial (0°) orbit.

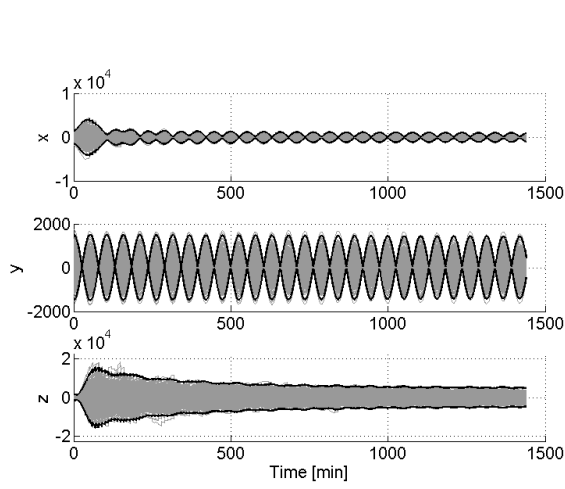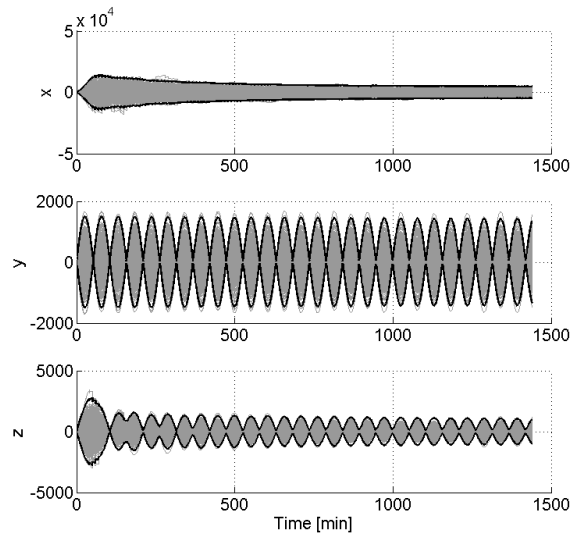(a) Position error [m] at i=45°.

(b) Velocity error [mm/s] at i=45°.

Figure 6: Monte Carlo position and velocity rrrors at 1,000 km 45°orbit.

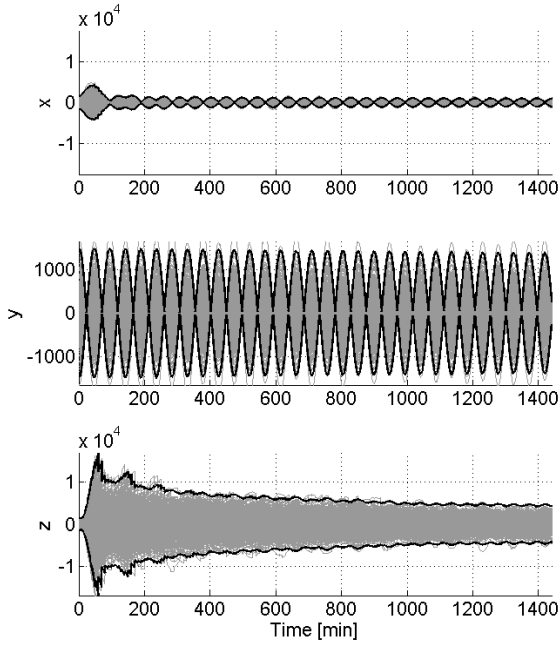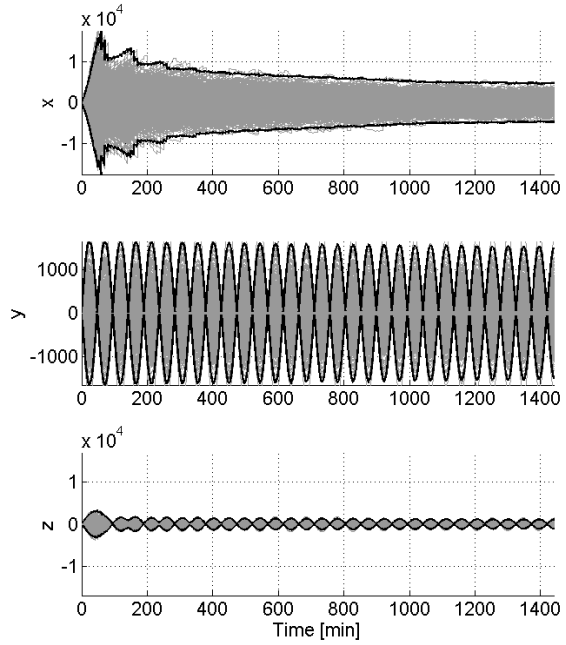American Institute of Aeronautics and Astronautics

(a) Position rrror [m] at i=90°.

(b) Velocity error [mm/s] at i=90°.

Figure 7: Monte Carlo position and velocity errors at 1,000 km polar (90°) orbit.

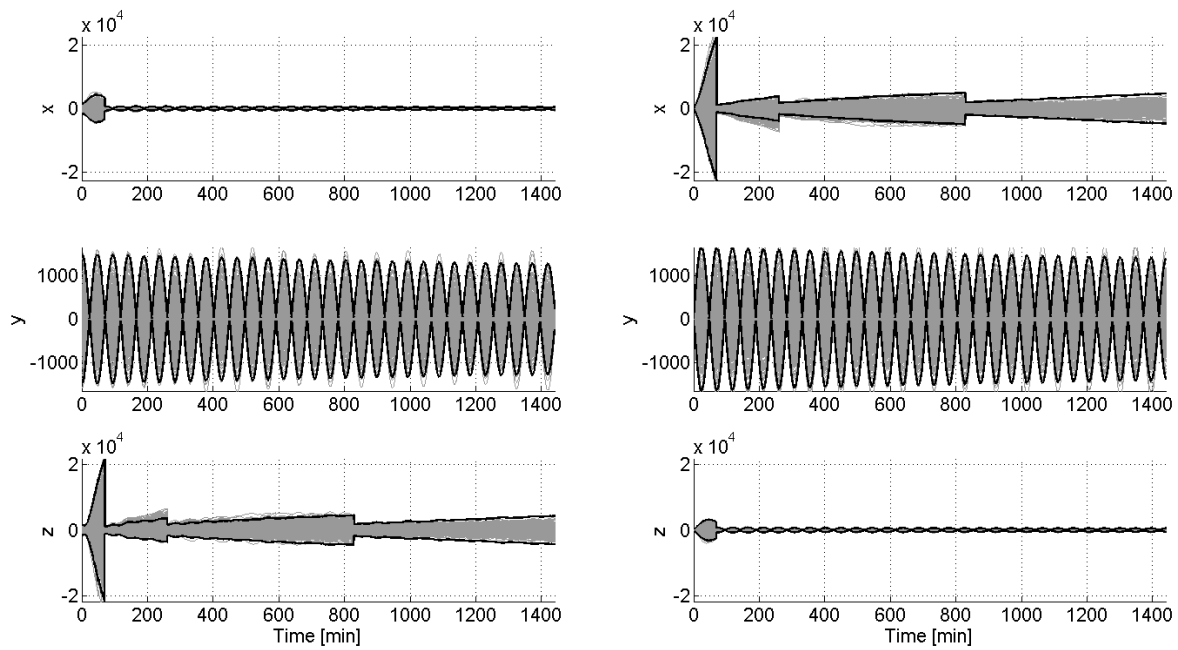(a) Position error [m] at i=45°.

(b) Velocity error [mm/s] at i=45°.

Figure 8: Monte Carlo position and velocity errors at 500 km 45°orbit.

American Institute of Aeronautics and Astronautics

(a) Position error [m] at i=90°.

(b) Velocity error [mm/s] at i=90°.

Figure 9: Monte Carlo position and velocity errors at 500 km polar (90°) orbit.

American Institute of Aeronautics and Astronautics

V.   Acknowledgments

References

[1] Christian, J. A. and Lightsey, E. G., "Onboard Image-Processing Algorithm for a Spacecraft Optical Navigation Sensor System," *Journal of Spacecraft and Rockets*, Vol. 49, No. 2, 2012, pp. 337–352.

[2] Owen, W., "Methods of Optical Navigation," *AAS Spaceflight Mechanics Conference*, No. AAS 11-215, New Orleans, LA, February 2011.

[3] Liu, H. and Jezek, K. C., "Automated Extraction of Coastline from Satellite Imagery by Integrating Canny Edge Detection and Locally Adaptive Thresholding Methods," *International Journal of Remote Sensing*, Vol. 25, No. 5, 2004, pp. 937–958.

[4] Cheng, Y. and Miller, J. K., "Autonomous Landmark Based Spacecraft Navigation System," *AAS/AIAA Astrodynamics Specialist Conference*, No. AAS 03-223, Ponce, Puerto Rico, February 2003.

[5] Rowell, N., Parkes, S., and Dunstan, M., "Image Processing for Near Earth Object Optical Guidance Systems," *IEEE Transactions on Aerospace and Electronic Systems*, Vol. 49, No. 2, 2013, pp. 1057–1072.

[6] Hanak, C., *Lost in Low Lunar Orbit Crater Pattern Detection and Identification*, Ph.D. thesis, University of Texas at Austin, 2009.

[7] Rohrschneider, R. R., "Terrain Relative Navigation Using Crater Identification in Surface Topography Data," *AIAA Guidance, Navigation, and Control Conference*, No. AIAA 2001-6490, Portland, Oregon, August 2011.

[8] Cheng, Y., Johnson, A. E., Matthies, L. H., and Olson, C. F., "Optical Landmark Detection for Spacecraft Navigation," *AAS/AIAA Astrodynamics Specialist Conference*, No. AAS 02-224, Ponce, Puerto Rico, February 2003.

[9] National Aeronautics and Space Administration, "Earth Features Seen From Space," May 1999.

[10] Canny, J., "A Computational Approach to Edge Detection," *IEEE Transactions on Pattern Analysis and Machine Intelligence*, Vol. 8, No. 6, 1986, pp. 679–698.

[11] Heene, G. and Gautama, S., "Optimisation of a Coastline Extraction Algorithm for Object-Oriented Matching of Multisensor Satellite Imagery," *IEEE Geoscience and Remote Sensing Symposium*, Vol. 6, 2000, pp. 2632–2634.

[12] Patt, F. S., Woodward, R. H., and Gregg, W. W., "An Automated Method for Navigation Assessment for Earth Survey Sensors using Target Islands," *International Journal of Remote Sensing*, Vol. 18, No. 16, 1997, pp. 3311–3336.

[13] Environmental Systems Research Institute, I., "ESRI Shapefile Technical Description," 1998.

[14] Sellers, J., *Understanding Space: An Introduction to Astronautics*, Learning Solutions.

[15] Gelb, A., *Applied Optimal Estimation*, The M.I.T. Press, Cambridge, MA, 1974.

[16] Brown, R. G. and Hwang, P. Y. C., *Introduction to Random Signals and Applied Kalman Filtering*, John Wiley and Sons, Inc., Hoboken, NJ, 1997.

[17] Shuster, M. D. and Oh, S. D., "Three-axis Attitude Determination from Vector Observations," *Journal of Guidance, Control, and Dynamics*, Vol. 4, No. 1, 1981, pp. 70–77.

[18] Liounis, A., Daniel, S., and Christian, J. A., "Autonomous Navigation System Performance in the Earth-Moon System," *AIAA Space Conference*, 2013.